Title
Error Analysis and Optimization of a Sky Full-Polarization Imaging Detection System

Journal
Photogrammetric Engineering & Remote Sensing, 87(4)

ISSN
0099-1112

Authors
Chen, Yongtai
Tang, William C
Chu, Jinkui
et al.

Publication Date
2021-04-01

DOI
10.14358/pers.87.4.273

Peer reviewed

Error Analysis and Optimization of a Sky Full-Polarization Imaging Detection System

Yongtai Chen[1,2,3], William C. Tang[3], Jinkui Chu[1,2], Ran Zhang[1,2], and Song Li[1,2]

[1]*Key Laboratory for Micro/Nano Technology and System of Liaoning Province, Dalian University of Technology, Dalian, China*
[2]*School of Mechanical Engineering, Dalian University of Technology, Dalian, China*
[3]*Department of Biomedical Engineering, University of California, Irvine, Irvine, CA, USA*

Abstract

An accurate sky polarization field map is a prerequisite for polarization navigation applications. In this article, a detector for sky full-polarization imaging detection is described, the major error-influencing factors (MEIFS) are obtained, and the error propagation is modeled and analyzed. We reveal the relationship between the error of the inversed Stokes vector and the condition number of the detector matrix, which shows that the error of the inversed Stokes vector is affected by the Stokes vector of the incident light itself and the MEIFS together, with the MEIFS playing a decisive role. With the MEIFS optimized, the impact of detector error on the inversed Stokes vector is attenuated. A control equation for system calibration is also deduced which can establish the connection between the detector matrix design and calibration process. The work in this article provides a reference for optimization and calibration of sky full-polarization imaging detectors.

Introduction

In recent years, a novel navigation method based on the sky polarization field map (SPFM) has become a research hot spot, expected to become an important supplement to traditional navigation methods (Karman, Diah and Gebeshuber 2012; Yan *et al.* 2018). Polarization navigation is a navigation method that uses sunlight (Yan *et al.* 2009) or moonlight (Cui *et al.* 2013) as a navigation beacon to obtain compass information by detecting and calculating the SPFM (Zhao *et al.* 2007). Figure 1 shows the theoretical SPFM under Rayleigh scattering in fine weather. Polarization navigation has the properties of insusceptibility to electromagnetic interference and artificial false-signal deception, as well as good independence. Its navigation and positioning functions have wide application value in military and civilian fields (Chu *et al.* 2016). Polarization navigation is also one of the navigation methods in nature (Chu *et al.* 2007; Chu *et al.* 2008; Chu *et al.* 2009). In 1985, the first research paper was published about the polarization navigation ability of sand ants (Fent and Wehner 1985).

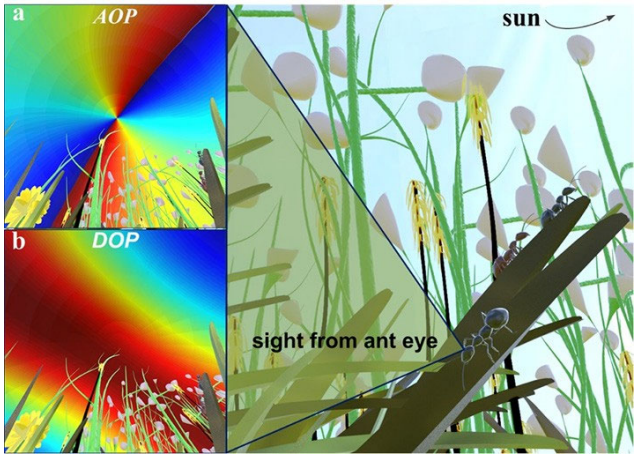

Figure 1. The theoretical sky polarization field map under Rayleigh scattering in fine weather.

In 2000, Lambrinos and colleagues (2000) applied the navigation strategy of desert ants to the autonomous navigation of mobile robots and obtained satisfactory experimental results, which verified the mechanism of biological polarization-sensitive navigation. Since then, many scholars have developed a series of polarization navigation sensors, which can be divided into two major categories: point-source polarization detectors (Chu and Zhao 2005; Cui *et al.* 2010; Liu *et al.* 2015; Wang *et al.* 2015; Chu *et al.* 2017) and imaging polarization detectors (Vedel, Breugnot and Lechocinski 2011;

Chahl and Mizutani 2012; Zhang, Zhao and Li 2013; Zhang *et al.* 2014; Lu *et al.* 2015). Point-source detectors are smaller, lower in cost, and easier to integrate and modify, but the distinction they capture is imperfect, making them unsuitable for applications in complex scenes. On the other hand, imaging polarization detectors have an abundant amount of information, which is beneficial to a variety of semantic processing tasks using the polarization image. They have good potential for making polarization data mining an important technical means for obtaining an SPFM. Many scholars have used their own imaging polarization detectors to study the SPFM under various weather conditions and obtained some meaningful conclusions. However, most of the current research focuses only on the linear polarization characteristics of the SPFM; analysis of the circular polarization characteristics has been neglected (Pomozi, Horváth and Wehner 2001; Pust *et al.* 2011). There is still knowledge of the SPFM to be explored in order to make this technology more flexible and stable for application. And to enrich the database information of the SPFM for further analysis, it is beneficial to expand the detection range of the Stokes vector from linear polarization to full polarization, which requires a full-polarization imaging detection system.

Hence, an optimized real-time full-polarization imaging detector was developed (Chen *et al.* 2018). Compared with other detectors, it has higher integration and portability, which will help to efficiently acquire an SPFM and to provide technical support for correcting and supplementing the theoretical model of polarization navigation. This system contains several polarization modulation components, where some deviations of the theoretical nominal parameters exist owing to manufacturing error, and these will introduce systematic error in the polarization inversion processing, thus affecting the detection robustness of the SPFM. There have not been reports of comprehensive study of the systematic error formation and optimization process of this detector. Based on the needs of future work, this article devises the error model of the system and obtains some important conclusions.

Establishment of the Detection System

Polarization Description and Calculation

The Stokes vector with an intensity base unit is one common method to describe polarization light (Hamaoui, 2017; Lu *et al.* 2017). The Stokes vector has four parameters – I, Q, U, and V, where $S = [I\ Q\ U\ V]^{\mathrm{T}}$:

$$S = \begin{bmatrix} I \\ Q \\ U \\ V \end{bmatrix} = \begin{bmatrix} I_{0^\circ} + I_{90^\circ} \\ I_{0^\circ} - I_{90^\circ} \\ I_{45^\circ} - I_{135^\circ} \\ I_R - I_L \end{bmatrix} \tag{1}$$

where I represents the total intensity of light, Q represents the intensity difference between the polarization components in the 0° and 90° directions, U represents the intensity difference between the polarization components in the 45° and 135° directions, and V represents the intensity difference between the right and left circular polarization components.

Each Stokes vector can be mapped onto the Poincaré sphere (Milione *et al.* 2011; Naidoo *et al.* 2016) as shown in Figure 2, where S_0 represents the total intensity of light, α is the azimuth, and β is the elliptic angle. Positive β indicates right-handed polarized light, so each point on the upper hemisphere represents right-handed polarized light, and correspondingly, each point on the lower hemispherical surface represents left-handed polarized light. Each point on the intersection of the spherical surface and the equatorial plane represents linearly polarized light, with $\beta = 0$. The upper and lower poles correspond to right-handed and left-handed circularly polarized light, respectively. The azimuth difference of the two polarized lights, which are symmetrical about the center of the Poincaré sphere, is 90°, and the absolute values of β are equal and with opposite signs, so a pair of orthogonally polarized lights is formed. The angle between two orthogonally linearly polarized lights is 90°, but on the spherical surface of the Poincaré sphere the corresponding points are located at symmetrical positions with an angle of π between them. The points inside the Poincaré sphere represent partially polarized lights. Thus, the points on the Poincaré sphere can represent polarized lights of any polarization state.

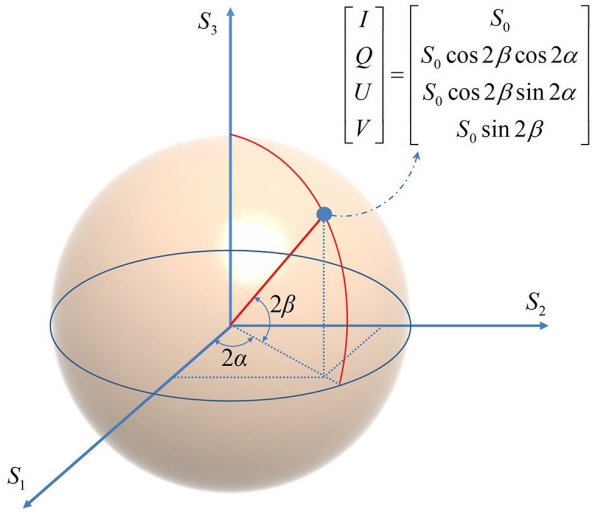

Figure 2. Poincaré sphere, onto which each Stokes vector can be mapped.

The four parameters of the Stokes vector can define different polarization characterization parameters (Zhang *et al.* 2015; Wu *et al.* 2018), called the SPFM when used in sky polarization detection. These are the angle of polarization (AOP), degree of polarization (DOP), degree of linear polarization (DOLP), and degree of circular polarization (DOCP), which are defined as follows:

$$AOP = \frac{1}{2}\arctan\left(\frac{U}{Q}\right) \tag{2}$$

$$DOP = \frac{\sqrt{Q^2 + U^2 + V^2}}{I} \tag{3}$$

$$DOLP = \frac{\sqrt{Q^2 + U^2}}{I} \tag{4}$$

$$DOCP = \frac{\sqrt{V^2}}{I} \tag{5}$$

Components of the System

In order to actualize the fully rationalized Mueller matrix of the system, which can help reduce computational cost, the optical modulator components with special parameters were selected to implement the optical path, mainly including three non-polarization beam-splitting prisms (Thorlabs), four non-polarization relay lenses (Edmund Optics), one quarter- wave plate (Thorlabs), and four polarizers (Edmund Optics), as shown in Figure 3 (left). A wide-angle (180°) fish-eye lens is installed at the entrance of the optical path, and four charge-coupled device (CCD) cameras are installed at the exit to realize simultaneous image acquisition. The host computer control program, which is developed based on MFC and OpenCV, helps to implement real-time solution and analysis of polarized images. To obtain the SPFM video stream, the images from the four CCD cameras undergo a series of image processing, including solving image registration relations, registering the video stream, selecting the image color channel, solving the Stokes vector, and solving the SPFM according to Equations 2–5. The detector is smaller than a basketball, which is beneficial for rapid deployment and for platform and field switching. The physical system is shown in Figure 3 (right), and the specific parameters of the detection system are shown in Table 1.

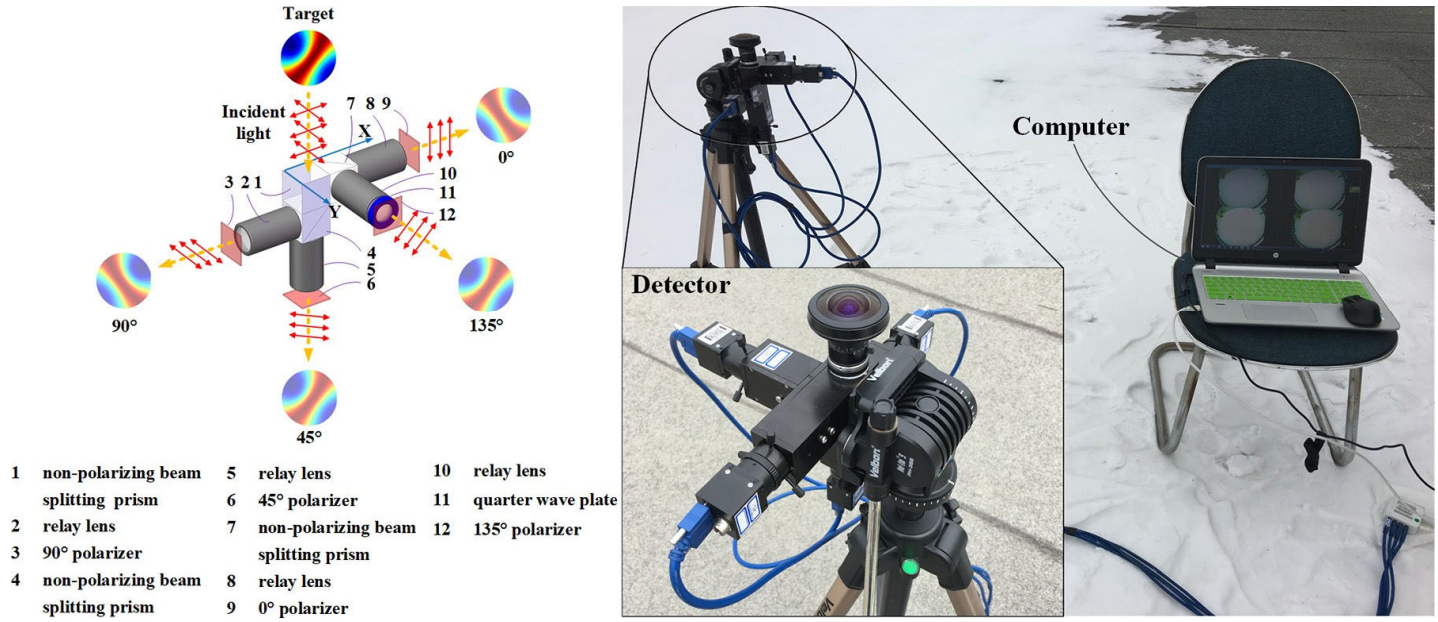

Figure 3. Schematic diagram of optical path and physical system.

Table 1. Main performance indicators of full-sky polarization imaging detector.

Indicator	Value
Resolution (pixels)	1024 × 1028
Bits/pixel	8
Field of view (°)	180
Frame rate (frames/s)	3
Spectral band (nm)	450–675

The theoretical Mueller matrix of the polarization detection system is

$$A_0 = \begin{bmatrix} 0.125 & 0.125 & 0 & 0 \\ 0.125 & 0 & 0.125 & 0 \\ 0.125 & -0.125 & 0 & 0 \\ 0.125 & 0 & 0 & -0.125 \end{bmatrix} \tag{6}$$

where i_0, i_1, i_2, and i_3 represent the image intensities obtained by the four CCDs, respectively. The column vector $I = [i_0\ i_1\ i_2\ i_3]^{\mathrm{T}}$ can be used to calculate the inversed Stokes vector S of the incident light:

$$S = \begin{bmatrix} I \\ Q \\ U \\ V \end{bmatrix} = A_0^{-1} I = \begin{bmatrix} 4 & 0 & 4 & 0 \\ 4 & 0 & -4 & 0 \\ -4 & 8 & -4 & 0 \\ 4 & 0 & 4 & -8 \end{bmatrix} \begin{bmatrix} i_0 \\ i_1 \\ i_2 \\ i_3 \end{bmatrix} \tag{7}$$

Error Analysis of the System

Major Error-Influencing Factors (MEIFs) of the System

The introduction of systematic errors in the derivation of the system Mueller matrix is mainly caused by the manufacturing error of the components and the positional deviation in the adjusting process, thus significantly affecting the inversion accuracy of the polarization characterization parameters. There are 10 MEIFs of the system: the transmittance k_1, k_2, k_3, and k_4 in each optical path; the polarizer mounting angles θ_1, θ_2, θ_3, and θ_4 in each optical path; the

mounting angle θ_5 of the fast axis of the quarter-wave plate; and the phase delay φ of the quarter-wave plate. All the MEIFs are shown in Table 2.

Table 2. The major error-influencing factors of the system.

	Factor									
Parameter Factor	k_1	k_2	k_3	k_4	θ_1	θ_2	θ_3	θ_4	θ_5	φ
Design Value	1/8	1/8	1/8	1/8	0°	45°	90°	135°	0°	$\pi/2$
Error range	−0.073 to −0.0015	−0.073 to −0.0015	−0.073 to −0.0015	−0.0782 to −0.0139	±5°	±5°	±5°	±5°	±5°	±λ/59

The design values of all MEIFs are determined according to the ideal parameters of the optical components in the detection system. The transmittance error in each optical path mainly comes from the deviation of the beam energy in the two orthogonal directions of the non-polarization beam-splitting prism, and it is calculated by the component data sheet from the official website of Thorlabs. As there is a quarter-wave plate in the fourth optical path, as shown in Figure 3 (left), the error range of k_4 is different from those of k_1, k_2, and k_3. According to a possible misalignment of the polarizers and the quarter-wave plate during installation, an error range of ±5° of the installation angles is produced. Based on the retardance accuracy (root-mean-square error [RMSE]) of the quarter-wave plate, the error range of the phase delay φ is obtained.

The design values of all MEIFs help to get the fully rationalized Mueller matrix A_0 of the system, but under the error impact of each MEIF, the actual Mueller matrix is not A_0, which can affect the accuracy of the inversed Stokes vector.

Error Propagation

In order to obtain accurate polarization characterization parameters such as AOP, DOP, DOLP, and DOCP, it is necessary to figure out the relationship between all MEIFs and the system Mueller matrix. The detection system consists of four optical paths, each of which has its own Mueller matrix:

$$M_1 = k_1 \begin{bmatrix} 1 & \cos 2\theta_1 & \sin 2\theta_1 & 0 \\ \cos 2\theta_1 & \cos^2 2\theta_1 & \sin 2\theta_1 \cos 2\theta_1 & 0 \\ \sin 2\theta_1 & \sin 2\theta_1 \cos 2\theta_1 & \sin^2 2\theta_1 & 0 \\ 0 & 0 & 0 & 0 \end{bmatrix} \tag{8}$$

$$M_2 = k_2 \begin{bmatrix} 1 & \cos 2\theta_2 & \sin 2\theta_2 & 0 \\ \cos 2\theta_2 & \cos^2 2\theta_2 & \sin 2\theta_2 \cos 2\theta_2 & 0 \\ \sin 2\theta_2 & \sin 2\theta_2 \cos 2\theta_2 & \sin^2 2\theta_2 & 0 \\ 0 & 0 & 0 & 0 \end{bmatrix} \tag{9}$$

$$M_3 = k_3 \begin{bmatrix} 1 & \cos 2\theta_3 & \sin 2\theta_3 & 0 \\ \cos 2\theta_3 & \cos^2 2\theta_3 & \sin 2\theta_3 \cos 2\theta_3 & 0 \\ \sin 2\theta_3 & \sin 2\theta_3 \cos 2\theta_3 & \sin^2 2\theta_3 & 0 \\ 0 & 0 & 0 & 0 \end{bmatrix} \tag{10}$$

$$M_4 = k_4 \begin{bmatrix} 1 & \cos 2\theta_4 & \sin 2\theta_4 & 0 \\ \cos 2\theta_4 & \cos^2 2\theta_4 & \sin 2\theta_4 \cos 2\theta_4 & 0 \\ \sin 2\theta_4 & \sin 2\theta_4 \cos 2\theta_4 & \sin^2 2\theta_4 & 0 \\ 0 & 0 & 0 & 0 \end{bmatrix} \times \begin{bmatrix} 1 & 0 & 0 & 0 \\ 0 & 1-(1-\cos\varphi)\sin^2 2\theta_5 & (1-\cos\varphi)\sin 2\theta_5 \cos 2\theta_5 & -\sin\varphi \sin 2\theta_5 \\ 0 & (1-\cos\varphi)\sin 2\theta_5 \cos 2\theta_5 & 1-(1-\cos\varphi)\cos^2 2\theta_5 & \sin\varphi \cos 2\theta_5 \\ 0 & \sin\varphi \sin 2\theta_5 & -\sin\varphi \cos 2\theta_5 & \cos\varphi \end{bmatrix} \tag{11}$$

$$\begin{cases} A_{error} = \begin{bmatrix} k_1 & k_1\cos 2\theta_1 & k_1\sin 2\theta_1 & 0 \\ k_2 & k_2\cos 2\theta_2 & k_2\sin 2\theta_2 & 0 \\ k_3 & k_3\cos 2\theta_3 & k_3\sin 2\theta_3 & 0 \\ k_4 & m_{42} & m_{43} & m_{44} \end{bmatrix} \\ m_{42} = k_4\cos 2\theta_4(\sin^2 2\theta_5(\cos\varphi - 1) + 1) - k_4\cos 2\theta_5\sin 2\theta_4\sin 2\theta_5(\cos\varphi - 1) \\ m_{43} = k_4\sin 2\theta_4(\cos^2 2\theta_5(\cos\varphi - 1) + 1) - k_4\cos 2\theta_4\cos 2\theta_5\sin 2\theta_5(\cos\varphi - 1) \\ m_{44} = k_4\cos 2\theta_5\sin 2\theta_4\sin\varphi - k_4\cos 2\theta_4\sin 2\theta_5\sin\varphi \end{cases} \tag{12}$$

In each optical path, the Stokes vector is modulated into a light intensity signal by the Mueller matrix M_1, M_2, M_3, or M_4 and recorded by the CCDs, respectively; then the first rows of M_1, M_2, M_3, and M_4 are extracted to form a new 4 × 4 matrix A_{error}, as shown in Equation 12. This matrix represents the actual system Mueller matrix under the impact of MEIFs. Equation 12 shows how each factor as an independent variable can affect the derivation process of the actual system Mueller matrix A_{error}.

In the real process of light transmission, the column vector I which is composed of the four image intensities is affected by A_{error}. But the theoretical Mueller matrix instead is brought into the actual inversion process, causing the error of the inversed incident Stokes vector, as follows:

$$I = A_{\text{error}}S_{\text{true}} \tag{13}$$

$$S_{\text{true}} = A_{\text{error}}^{-1}I \tag{14}$$

$$S' = A_0^{-1}I \tag{15}$$

where $S_{\text{true}} = [I\ Q\ U\ V]^{\text{T}}$ is the true Stokes vector of the incident light and S' is the inversed Stokes vector with the error. The error transmission process of the system can be deduced from Equations 13–15:

$$\begin{aligned} \Delta S = S_{\text{true}} - S' &= \left(A_{\text{error}}^{-1} - A_0^{-1}\right)A_{\text{error}}S_{\text{true}} = \left(A_{\text{error}}^{-1}A_{\text{error}} - A_0^{-1}A_{\text{error}}\right)S_{\text{true}} \\ &= \left(E - A_0^{-1}A_{\text{error}}\right)S_{\text{true}} = \left(A_0^{-1}A_0 - A_0^{-1}A_{\text{error}}\right)S_{\text{true}} = A_0^{-1}(A_0 - A_{\text{error}})S_{\text{true}} \\ &= A_0^{-1}\Delta A S_{\text{true}} \end{aligned} \tag{16}$$

where $\Delta S = [\Delta I\ \Delta Q\ \Delta U\ \Delta V]^{\text{T}}$ is the error of the Stokes vector of the incident light.

Then, according to Equation 6, 7, 12, and 16, the relationship between the error in the Stokes vector of the incident light and all MEIFs can be revealed:

$$\begin{bmatrix} \Delta I \\ \Delta Q \\ \Delta U \\ \Delta V \end{bmatrix} = \begin{bmatrix} 1 - 4k_1 - 4k_3 & -4k_1\cos 2\theta_1 - 4k_3\cos 2\theta_3 & -4k_1\sin 2\theta_1 - 4k_3\sin 2\theta_3 & 0 \\ -4k_1 + 4k_3 & 1 - 4k_1\cos 2\theta_1 + 4k_3\cos 2\theta_3 & -4k_1\sin 2\theta_1 + 4k_3\sin 2\theta_3 & 0 \\ 4k_1 - 8k_2 + 4k_3 & 4k_1\cos 2\theta_1 - 8k_2\cos 2\theta_2 + 4k_3\cos 2\theta_3 & 1 + 4k_1\sin 2\theta_1 - 8k_2\sin 2\theta_2 + 4k_3\sin 2\theta_3 & 0 \\ -4k_1 - 4k_3 + 8k_4 & -4k_1\cos 2\theta_1 - 4k_3\cos 2\theta_3 + 8m_{42} & -4k_1\sin 2\theta_1 - 4k_3\sin 2\theta_3 + 8m_{43} & 1 + 8m_{44} \end{bmatrix} \begin{bmatrix} I \\ Q \\ U \\ V \end{bmatrix} \tag{17}$$

In Equation 16 and 17, ΔS is affected by the incident Stokes vector and MEIFs together. In order to figure out the range of ΔS that can be accepted, and to ascertain the calibration strategy of the system Mueller matrix, a simulation was conducted. The polarized light used in the simulation was full-polarization light. Through comparison analysis, we found that when the values of ΔI, ΔQ, ΔU, and ΔV are within ±0.005, the RMSE of DOP, DOLP, and DOCP are less than 0.5%, as shown in Figure 4b. As for the RMSE of AOP, 99% of it is less than 1º, with 75% less than 0.25º, as shown in Figure 4a. The incident Stokes vector corresponding to the 1% of AOP data with RMSE greater than 1º mainly distributes on the surface of the Poincaré sphere, where S1 is greater than 0, as shown in Figure 4c. The SPFM is one of the targets with low-frequency change (Zhang *et al.* 2015), and therefore its geometric features have a relatively high noise tolerance. The detection requirements of the SPFM can be basically satisfied by controlling the values of ΔI, ΔQ, ΔU, and ΔV within ±0.005.

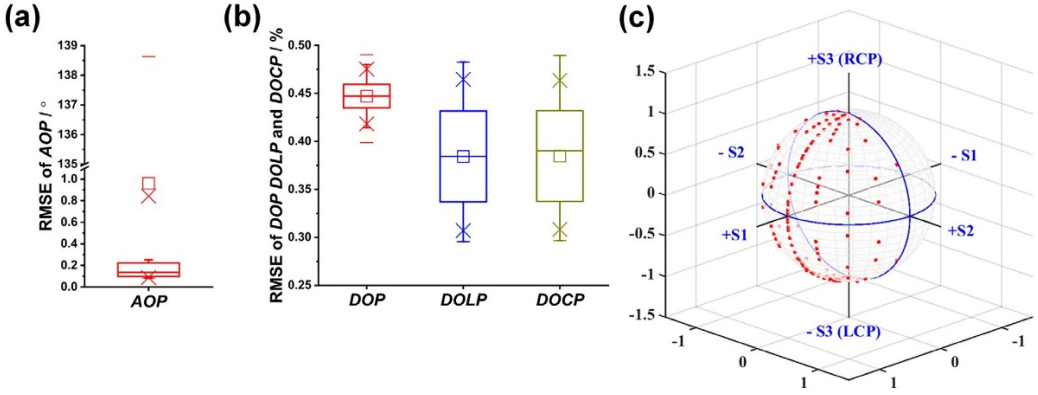

Figure 4. (a) Root-mean-square error (RMSE) distribution of AOP. (b) RMSE distribution of DOP, DOLP, and DOCP. (c) Poincaré sphere distribution of the incident Stokes vector corresponding to the 1% of AOP data with RMSE greater than 1°

In Equation 18, the 2-norm (Tyo 2002) of ΔS represents the Euclidean distance between S_{true} and S', and it can be used to assess the extent to which S' deviates from S_{true}:

$$D(S_{\text{true}}, S') = \left\|\Delta S\right\|_2 = \sqrt{(\Delta I)^2 + (\Delta Q)^2 + (\Delta U)^2 + (\Delta V)^2} \tag{18}$$

The matrix condition number (Vaughn and Hoover 2008; Foster *et al.* 2015; Bruce et al. 2018) is the key parameter to evaluate the degree of morbidity of the system matrix; $K(A_{\text{error}})$ is the system matrix condition number with error, it is defined as

$$K(A_{\text{error}}) = \left\|A_{\text{error}}\right\| \left\|A_{\text{error}}^{-1}\right\| \tag{19}$$

There are many possible combinations of MEIFs, producing different condition numbers of A_{error}. One special situation is that different combinations of MEIFs may produce the same condition number of A_{error}. For each combination of MEIFs, the polarization state of the incident light is set using the Stokes vectors that map the entire Poincaré sphere, and the $D(S_{\text{true}}, S')$ distribution of the inversed Stokes vector under the impact of MEIFs is computed according to Equations 16–19 and then the average value and standard deviation (SD) of $D(S_{\text{true}}, S')$ are calculated. After analyzing the $D(S_{\text{true}}, S')$ distribution under different MEIF combinations, we obtained the impact of the system matrix condition number with error and the incident polarization state on the detection accuracy. It can be seen in Figure 5 that the system matrix condition number with error ranges from 2.78 to 5.06, with an average of 3.84. The blue points represent the average value of $D(S_{\text{true}}, S')$ under different matrix condition numbers, and the value range is between 0.22 and 0.88, while the red points represent the SD of $D(S_{\text{true}}, S')$, with values ranging from 0.02 to 0.38. The average and SD data of $D(S_{\text{true}}, S')$ reflect that the final accuracy of the polarization detection system is affected by both MEIFs and the polarization state of the incident light.

Taking one set of data points as a sample, it can be seen from Figure 5a that $D(S_{\text{true}}, S')$ of the sample point has a large value range, between 0.13 and 0.97, as it has a uniquely determined matrix A_{error}, and the influence on $D(S_{\text{true}}, S')$ is mainly from the polarization state of the incident light. The respective trend lines (solid red and blue lines) are plotted according to the clustering and distribution patterns of mean and SD points, qualitatively showing that the condition number of A_{error} and the mean and SD of $D(S_{\text{true}}, S')$ are positively correlated, which indicates that the condition number of A_{error} plays a dominant role in determining $D(S_{\text{true}}, S')$. Hence, it is possible to control the $D(S_{\text{true}}, S')$ error by diminishing the condition number of the system matrix through optimizing the MEIFs. The condition number of the theoretical system matrix designed in this article is 3.2255. As shown in Figure 5, under the influence of MEIFs, about 20% of the condition numbers are smaller than the theoretical matrix condition number, which indicates that in some combinations, MEIFs can produce a self-optimization effect on the system matrix condition number, to a maximum degree of 13.8%; however, this effect is not stable. And one condition number can correspond to different numerical distributions of $D(S_{\text{true}}, S')$, which indicates that the same condition number with different MEIFs has differential sensitivity to the incident polarization state. This randomness impairs the self-optimization effect of MEIFs on the system matrix, so it is necessary to avoid such randomness.

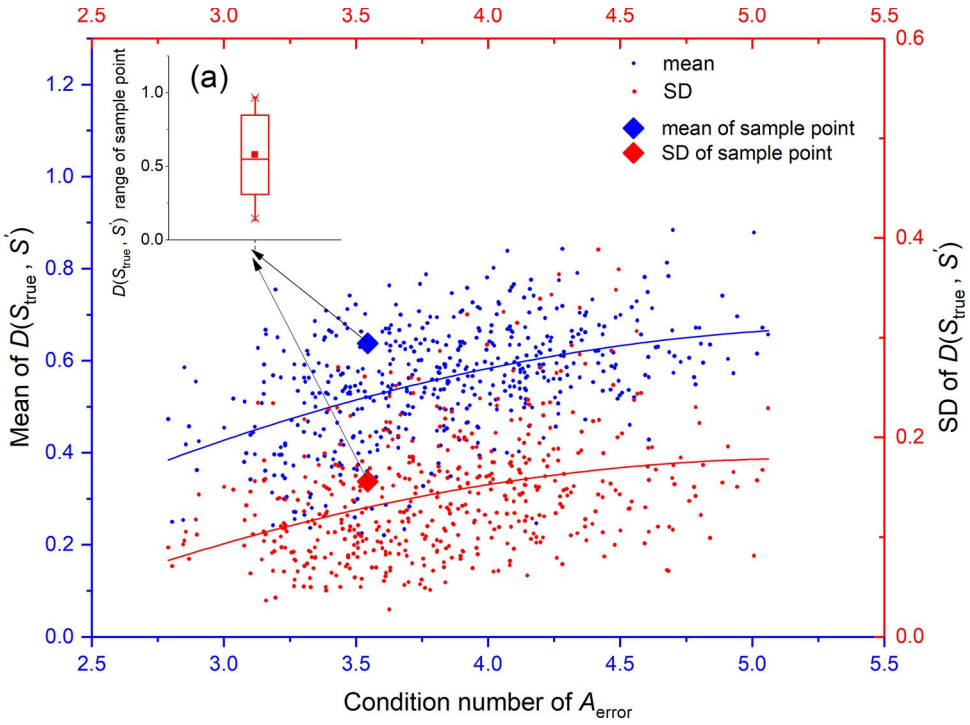

Figure 5. Influence of system matrix condition number with error and incident polarization state on detection accuracy.

Optimization of System Parameters

According to the compatibility of norms, from Equation 16 we can deduce

$$D(S_{\text{true}}, S') \le \left\|A_0^{-1}\right\|_2 \left\|\Delta A\right\|_2 \left\|S_{\text{true}}\right\|_2 \le \sqrt{2}\left\|A_0^{-1}\right\|_2 \left\|\Delta A\right\|_2 \tag{20}$$

The maximum value of $D(S_{\text{true}}, S')$ can be constrained by three factors, namely the 2-norms of A_0^{-1}, ΔA, and S_{true}, where $\left\|S_{\text{true}}\right\|_2 \le \sqrt{2}$ under normalized condition and $D(S_{\text{true}}, S')$ is normalized as S_{true}. Intuitively, A_0 can affect the 2-norm of A_0^{-1} and ΔA at the same time, indicating that the degree of the randomness already mentioned is mainly caused by the theoretical Mueller matrix A_0. It is possible to control the $D(S_{\text{true}}, S')$ variation by optimizing the MEIFs of the system matrix.

There are 10 MEIFs, and their relationship to $D(S_{\text{true}}, S')$ is highly coupled. Considering cost control and implementation difficulty, without replacing existing system components, the optimizable parameters are mainly the mounting angles of the polarizers and quarter-wave plate θ_1, θ_2, θ_3, θ_4, and θ_5. The flowchart of the optimization process is shown in Figure 6.

The steps of the optimization process are as follows:

1. Set k_1, k_2, k_3, k_4, and φ as design values, as shown in Table 2.
2. Set the angular optimization ranges for θ_1, θ_2, θ_3, θ_4, and θ_5 as [0, π], the step length of angular optimization for θ_1, θ_2, θ_3, θ_4, and θ_5 as L, and the number of optimizations per angle as π/L + 1.
3. Traverse θ_1, θ_2, θ_3, θ_4, and θ_5 in [0, π]:
    a. Set θ_1, θ_2, θ_3, and θ_4 as initial value 0 and traverse θ_5 with step L.
    b. Traverse θ_4 with step L, and traverse θ_5 with step L once for each additional L in θ_4.
    c. Traverse θ_3 with step L, and repeat step (b) for each additional L in θ_3.
    d. Traverse θ_2 with step L, and repeat step (c) for each additional L in θ_2.
    e. Traverse θ_1 with step L, and repeat step (d) for each additional L in θ_1.
4. Calculate the condition number CN of the system matrix for each value of θ_1, θ_2, θ_3, θ_4, and θ_5.
5. Calculate the minimum of CN, and list the corresponding θ_1, θ_2, θ_3, θ_4, and θ_5 values.

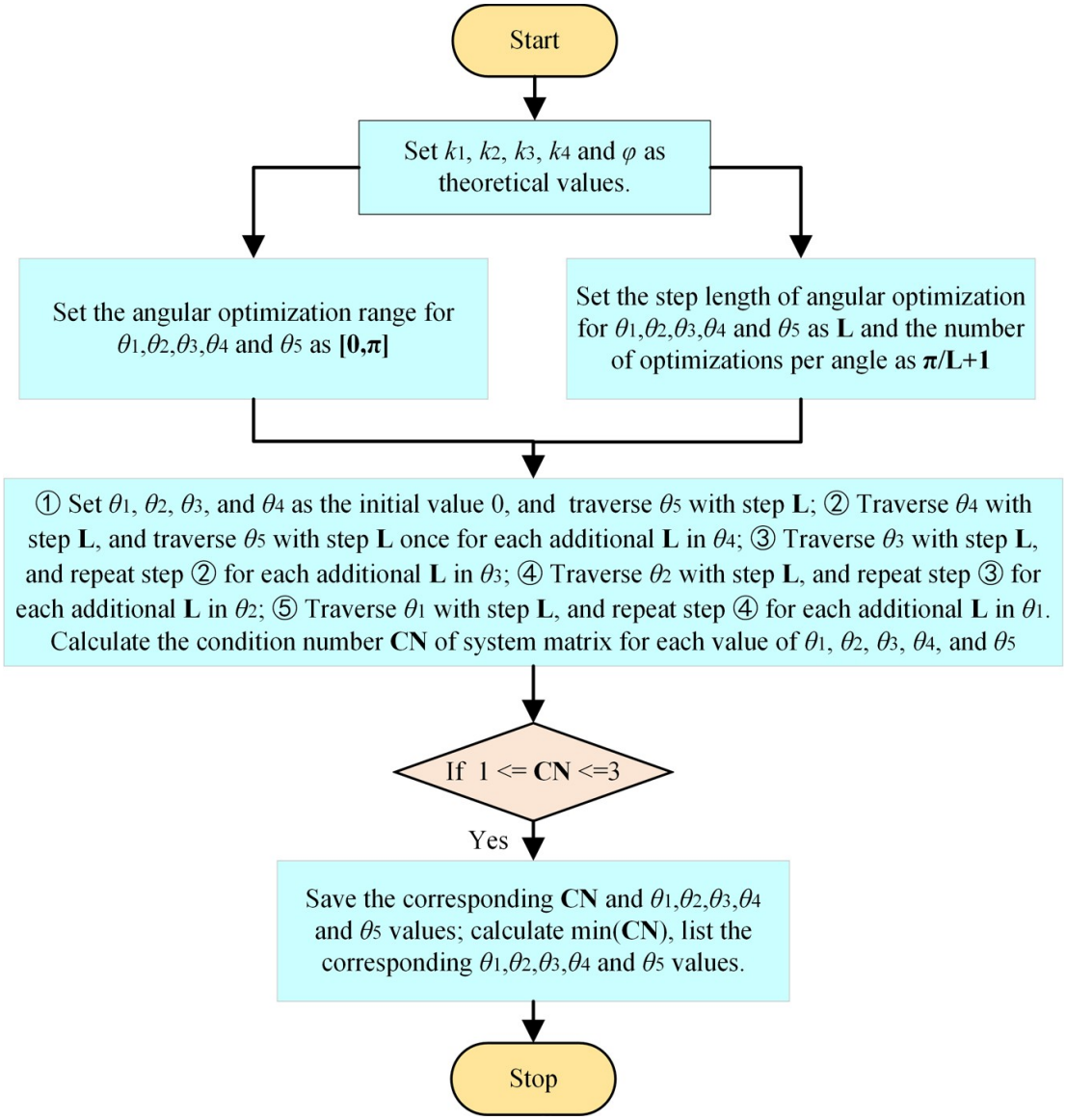

Figure 6. Flowchart of optimization process for θ_1, θ_2, θ_3, θ_4, and θ_5.

Through this simulation, 840 sets of optimal combinations of θ_1, θ_2, θ_3, θ_4, and θ_5 values were generated. The property of the elementary transformation of a matrix indicates that after adjusting the order of the rows, a changed matrix is equivalent to the original one, and we also verified that the condition number of the matrix would not change. Equations 8–10 are formally similar, so the optimal combinations of θ_1, θ_2, and θ_3 can neglect their sequence; θ_4 and θ_5 are the angles of the polarizer and the quarter-wave plate in the same optical path, and they are physically sequentially related and need to be listed separately. Thus, 840 sets of the optimal combinations can be categorized into 96 sets, as shown in Table 3. In this simulation, θ_5 gets 12 optimal values, and each value can correspond to two optimal values of θ_4 and four combinations of θ_1, θ_2, and θ_3. For example, when $\theta_5 = 0°$, θ_4 equals either 45° or 135°, and the combination of (θ_1, θ_2, θ_3) can be (0°, 60°, 120°), (15°, 75°, 135°), (30°, 90°, 150°), or (45°, 105°, 165°).

With the optimized combinations in Table 3, the condition number of the theoretical system matrix can be diminished from 3.2255 to 2.4842, a reduction of approximately 30%, and the 2-norm of A^{-1} is decreased from 12.0818 to 9.5808, a reduction of approximately 20.7%, which indicates that the influence of the MEIFs on $D(S_{true}, S')$ variation can be reduced to some extent. Although the optimized combinations of θ_1, θ_2, θ_3, θ_4, and θ_5 are obtained, these ideal combinations may still be affected by the MEIFs in Table 2 during the actual assembly of the system, thus leading to biases in solving the Stokes vector as well. To this end, the effect of the MEIFs on the condition number of the actual matrix A_{error} and $D(S_{true}, S')$ variation was simulated, with the ideal Mueller matrix A_0 being the optimized one in these analyses.

Table 3. 96 combinations of θ_1, θ_2, θ_3, θ_4, and θ_5 with the condition number optimized to 2.4842.

Subgroups of (θ_1, θ_2, θ_3)	θ_4	θ_5
Combinations of optimized angles (0°, 60°, 120°) (15°, 75°, 135°) (30°, 90°, 150°) (45°, 105°, 165°)	45° or 135°	0°
	60° or 150°	15°
	75° or 165°	30°
	0° or 90°	45°
	15° or 105°	60°
	30° or 120°	75°
	45° or 135°	90°
	60° or 150°	105°
	75° or 165°	120°
	0° or 90°	135°
	15° or 105°	150°
	30° or 120°	165°

Twenty-four out of 96 combinations of θ_1, θ_2, θ_3, θ_4, and θ_5 were selected for analysis, corresponding to all cases of θ_4 and θ_5 and one subgroup each of θ_1, θ_2, and θ_3, respectively. The case before optimization is denoted "ori," and opt1 through opt24 represent the cases after optimization. In Figure 7, the optimized condition number of A_{error} decreases considerably, with the average, 75% fraction, and 95% fraction all smaller than before optimization, and the optimized averages are almost at the same level, indicating that the optimized ideal Mueller matrix A_0 can diminish the negative effect of MEIFs on the condition number of A_{error}.

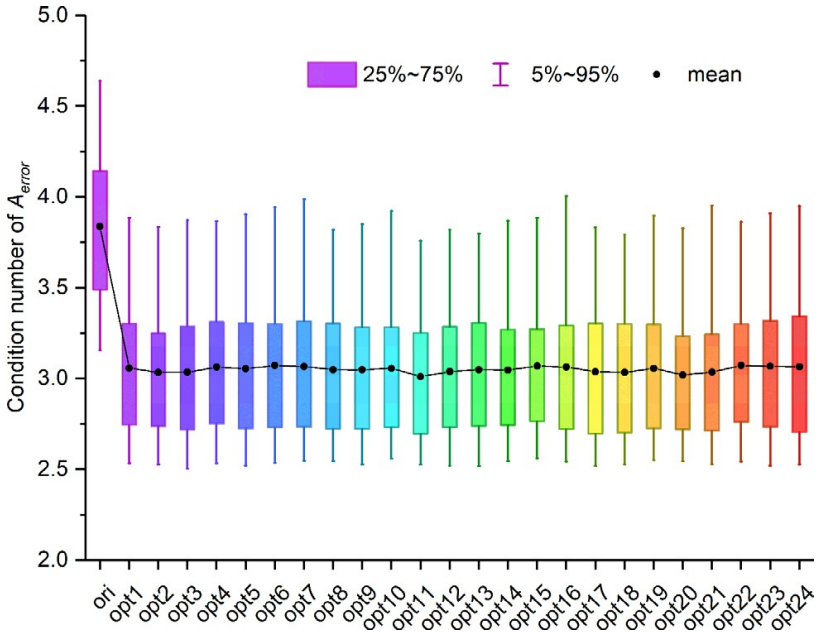

Figure 7. Comparison of condition number of A_{error} before and after optimization. Before optimization = ori; after optimization = opt1–opt24.

Figures 8 and 9 show the effect of MEIFs on $D(S_{\text{true}}, S')_{\text{mean}}$ and $D(S_{\text{true}}, S')_{\text{SD}}$ before and after optimization. In Figure 8, the optimized $D(S_{\text{true}}, S')_{\text{mean}}$ has the same average and confidence interval, and the average is smaller than before optimization. Taking ori and opt11 as examples, the normal probability plots show that the $D(S_{\text{true}}, S')_{\text{mean}}$ for opt11 as a whole indicates a relatively smaller value distribution than for ori. In Figure 9, the average values of almost all optimized $D(S_{\text{true}}, S')_{\text{SD}}$ are smaller than before optimization, and the normal probability plots also show that the $D(S_{\text{true}}, S')_{\text{SD}}$ for opt11 has a relatively smaller numerical interval than for ori. Figures 8 and 9 both indicate that the optimized MEIFs have an attenuated effect on $D(S_{\text{true}}, S')$ to some extent.

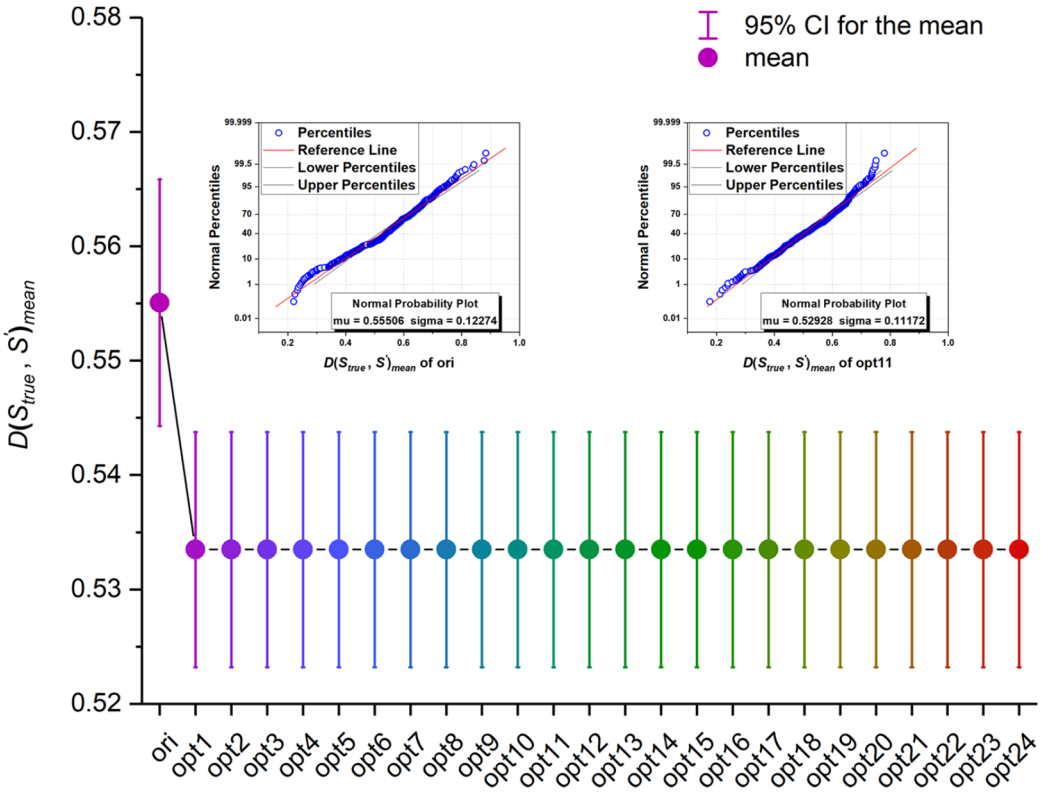

Figure 8. Comparison of $D(S_{true}, S')_{mean}$ before and after optimization. $D(S_{true}, S')_{mean}$ is the average of $D(S_{true}, S')$. Before optimization = ori; after optimization = opt1–opt24.

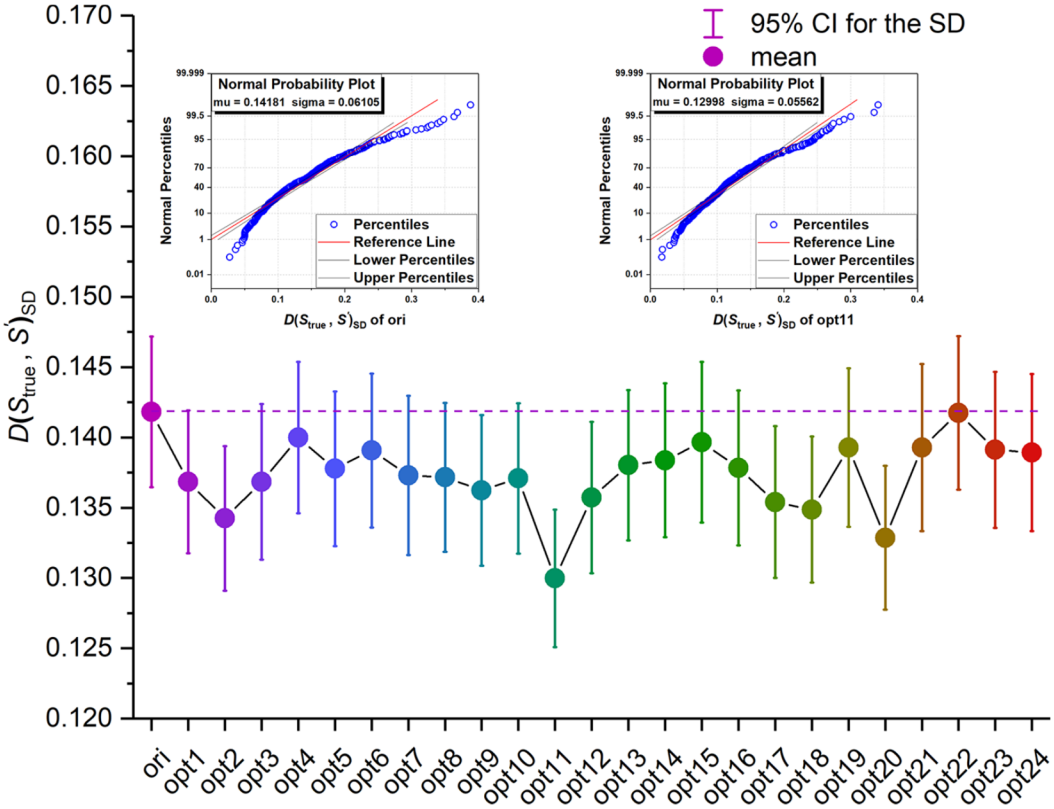

Figure 9. Comparison of $D(S_{true}, S')_{SD}$ before and after optimization. $D(S_{true}, S')_{SD}$ is the SD of $D(S_{true}, S')$. Before optimization = ori; after optimization = opt1–opt24.

Relationship Between System Design and Calibration

When the values of ΔI, ΔQ, ΔU, and ΔV are within ±0.005, $D(S_{\text{true}}, S')_{\max} = 0.01$. Using $D(S_{\text{true}}, S')$ to assess the extent to which S' deviates from S_{true}, the uncertainty of the precision control of the incident Stokes vector is replaced by a certain value $D(S_{\text{true}}, S')_{\max}$. The calibration accuracy control formula can be deduced from Equation 20 as

$$\left\|\Delta A\right\|_2 \le \frac{D(S_{\text{true}}, S')_{\max}}{\sqrt{2}\left\|A_0^{-1}\right\|_2} = \frac{0.01}{\sqrt{2}\left\|A_0^{-1}\right\|_2} \tag{21}$$

Equation 21 contains three variables: $\left\|A_0^{-1}\right\|_2$ reflects the design accuracy of the polarization detection system, $\left\|\Delta A\right\|_2$ reflects the control accuracy of the calibration system, and $D(S_{\text{true}}, S')_{\max}$ reflects the maximum value of $D(S_{\text{true}}, S')$. The equation links the two mutually independent design processes of the polarization detection system and the calibration system. Designing and implementing the calibration system according to Equation 21 can help to examine the required accuracy of the polarization detection system, and the value of $D(S_{\text{true}}, S')_{\max}$ can also be set according to the inversed Stokes vector accuracy.

Calibration Analysis and Experiments

Calibration Analysis

Equation 16 and Figure 5 show that the accuracy of the inversed Stokes vector is affected by the incident polarization state itself and the MEIFs together. Equation 21 is deduced and the calibration accuracy control formula is obtained. In Equation 21, $\left\|\Delta A\right\|_2$ reflects the control accuracy of the calibration system. However, $\left\|\Delta A\right\|_2$ can be further divided into two parts:

$$\Delta A = \Delta A_m + \Delta A_c \tag{23}$$

$$\left\|\Delta A\right\|_2 = \left\|\Delta A_m + \Delta A_c\right\|_2 \le \left\|\Delta A_m\right\|_2 + \left\|\Delta A_c\right\|_2 \tag{24}$$

where ΔA_m represents the error introduced by the optics components in the detection system and ΔA_c represents the error introduced by the calibration system. According to Equations 21–23, with a certain $D(S_{\text{true}}, S')_{\max}$, the smaller the $\left\|A_0^{-1}\right\|_2$, the lower the limit of $\left\|\Delta A\right\|_2$, which means that the error tolerance of the detection system and the calibration system is higher.

Technically, one way to reduce ΔA_m is to precisely adjust the optics components in the detection system according to the theoretical parameters, but this is difficult. The value of ΔA_c is mainly generated from the light source section of the calibration system. For a full-polarization calibration system, the polarized light generator mainly includes an integrating sphere, a polarizer, and a wave plate. A variety of polarized incident light can be generated by changing the polarizing angle ζ of the polarizer and the fast axis angle η of the wave plate. However, ζ and η will dynamically change in operation, and even a small $\Delta\zeta$ or $\Delta\eta$ can change the polarization state of the incident light and introduce calibration error in the fitting solution of the Mueller matrix. In order to eliminate dynamic error of ζ and η, high-precision motorized turntables are required to rotate the polarizer and wave plate. Also, $\Delta\zeta$, $\Delta\eta$, and the initial values of ζ_0 and η_0 should be treated as parameters to be calibrated, which can be fitted together with the Mueller matrix of the detection system to eliminate ΔA_c and ΔA_m. Based on these considerations, the method used in the calibration was the nonlinear least-squares fit (NLSF), which is a tool for solving multi-parameter nonlinear problems.

Experiments

The nonlinear least-squares fit method was used to calibrate the system. The calibration process includes an integrating sphere light source, a modulation unit of the incident light polarization, and the full-polarization imaging detection system. The modulation unit consists of a 532-nm filter, a high-precision motorized turntable, a polarizer, a precision angle sensor, and a quarter-wave plate, in sequence. The polarizer is mounted on the turntable, and the quarter-wave plate is on the angle sensor. The main calibration steps are as follows:

1. There are 10 MEIFs in the detection system, and the purpose of the calibration is to get the accurate detector system matrix **M**, so the 16 elements of **M** can represent the MEIFs in the calculation. Then 20 unknown parameters of the calibration process are determined: the 16 elements of the detector system matrix **M** and four other parameters of the modulation unit – the transmittance τ, the initial angles ζ_0 and η_0 of the polarizer and quarter-wave plate, and the phase delay Δ of the quarter-wave plate.

2. Rotate the quarter-wave plate in the modulation unit from 0° to 360° at 45° intervals. With each angle of the quarter-wave plate, rotate the polarizer from 0° to 360° at 45° intervals to create polarized incident light, and record all 64 sets of data with the detector.

3. Applying the nonlinear least-squares fitting method, fit the above 20 parameters.

4. According to the fitted initial angle ζ_0 of the polarizer, use the high-precision motorized turntable to adjust the polarizer direction to 0°. Remove the quarter-wave plate from the modulation unit, vary the polarizer direction from 0° to 170°, and record every 10° by the detection system, for a total of 18 sets.

5. Add the quarter-wave plate and angle sensor behind the polarizer and adjust the direction of the fast axis of the wave plate to 0° according to the fitted value η_0. Adjust the polarizer direction to −45° to create the right-hand circularly polarized light, and record it by the detection system.

6. Repeat (5) for a total of seven times.

7. Calculate AOP, DOLP, and DOCP of the linearly and circularly polarized incident light using the system matrix before and after calibration. Compare the errors with the created known polarized light. Results are shown in Figures 10–12.

Figures 10 and 11 show the AOP and DOLP of the linearly polarized incident light calculated by the detection system before and after the NLSF calibration. The detection errors of AOP and DOLP are less than 0.2° and 2.5%, respectively, after the calibration. Figure 12 shows the DOCP of right-handed circularly polarized incident light calculated by the detection system before and after the NLSF calibration. The detection error of DOCP is less than 3.6% after the calibration. The errors in AOP, DOLP, and DOCP are all reduced by approximately 50% with the NLSF method, compared with the calibration method without ζ and η as fitting parameters.

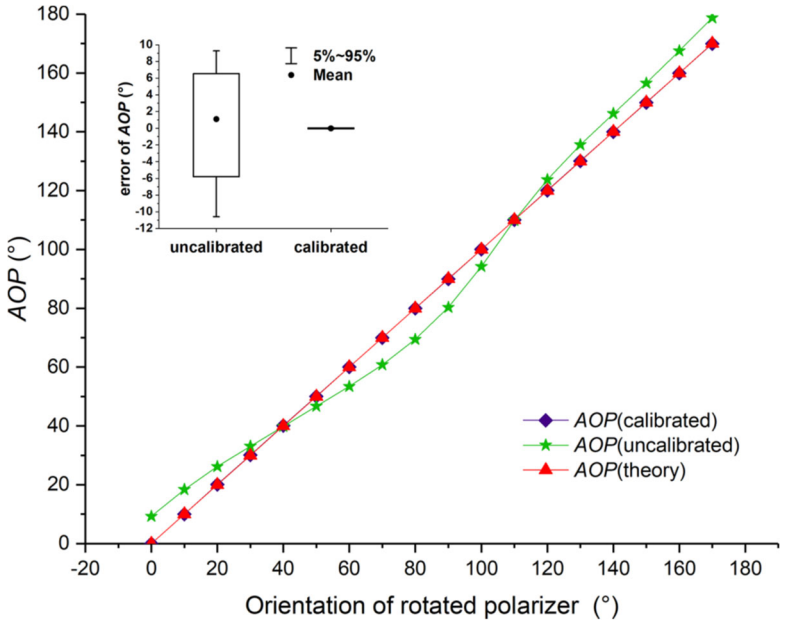

Figure 10. Difference in AOP before and after calibration. Subgraph: error of AOP (°) uncalibrated and calibrated.

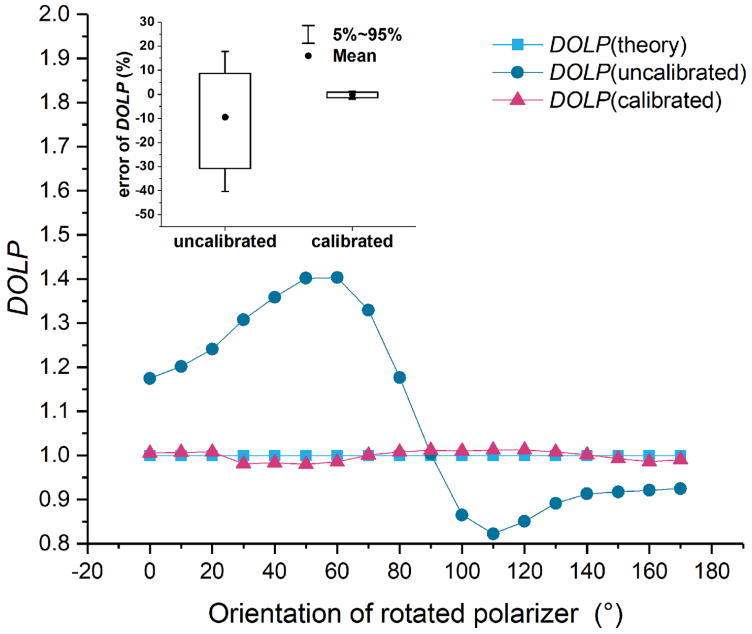

Figure 11. Difference in DOLP before and after calibration. Subgraph: error of DOLP (%) uncalibrated and calibrated.

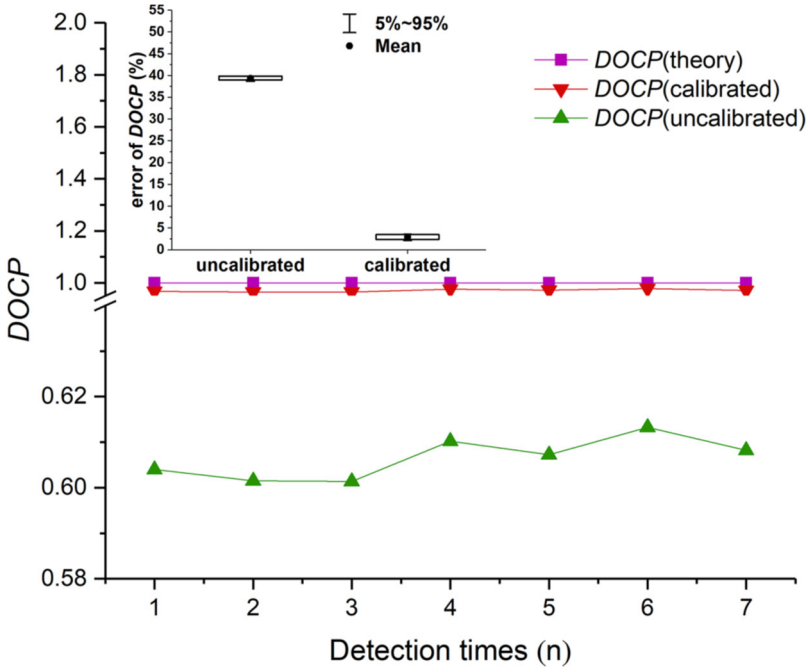

Figure 12. Difference in DOCP before and after calibration. Subgraph: error of DOCP (%) uncalibrated and calibrated.

Conclusions and Future Work

In this article, the MEIFs of the full-polarization detection system were analyzed, the error propagation process was derived, and the detection system was calibrated. In summary, the error propagation process indicates that the error of the inversed Stokes vector is affected both by MEIFs and by the polarization state of the incident light. By applying the 2-norm of the Stokes vector and the condition number of the system Mueller matrix as the evaluation criteria of detection accuracy and MEIF impact, respectively, we found that MEIFs dominate the formation of detection error, and their relationship is positively correlated, so the detection error can be controlled by attenuating the condition number of the system matrix while designing the detection system.

After the optimization of θ_1, θ_2, θ_3, θ_4, and θ_5, 96 sets of angle combinations were obtained with smaller matrix condition numbers, and the analyses indicate that the optimal combinations can diminish the negative effect of MEIFs and the polarization state of the incident light on the detection accuracy. Under the acceptable error range of the inversed Stokes vector, the control equation of system calibration was ascertained, which can help to examine the design and calibration of the detection system. The work in this article provides a reference for the optimization and calibration of full-polarization imaging detectors.

Acknowledgments

This work was supported by the National Natural Science Foundation of China (51675076, 51505062), the Science Fund for Creative Research Groups of the National Natural Science Foundation of China (51621064), and the Pre-Research Foundation of China (61405180102).

References

Bruce, N. C., J. M. López-Téllez, O Rodríguez-Núñez and O. G. Rodríguez-Herrera. 2018. Permitted experimental errors for optimized variable-retarder Mueller-matrix polarimeters. *Optics Express* 26 (11):13693–13704.

Chahl, J. and A. Mizutani. 2012. Biomimetic attitude and orientation sensors. *IEEE Sensors Journal* 12 (2):289–297.

Chen, Y.-T., R. Zhang, W. Lin and J.-K. Chu. 2018. Design and construction of real-time all-polarization imaging detector for skylight. *Optics and Precision Engineering* 26 (4):816–824.

Chu, J., H. Wang, W. Chen and R. Li. 2009. Application of a novel polarization sensor to mobile robot navigation. Pages 3763– 3768 in *2009 International Conference on Mechatronics and Automation*, held in Changchun, China, 9–12 August 2009. Edited by J. Editor. City, St.: IEEE.

Chu, J.-K., H.-X. Zhang, Y.-L. Wang and C. Shi. 2017. Design and construction of autonomous real-time position prototype based on multi-polarized skylight. *Optics and Precision Engineering* 25 (2):312–318.

Chu, J., R. Zhang, Z. Wang and Y. Wang. 2016. Progress on bio- inspired polarized skylight navigation sensor. *Chinese Science Bulletin* 61 (23):2568–2577.

Chu, J.-K. and K.-C. Zhao. 2005. Study of angle measurement optoelectronic model on emulating polarization-sensitive compound eye of insect. *Micronanoelectronic Technology* 42 (12):541–545.

Chu, J., K. Zhao, T. Wang and Q. Zhang. 2007. Research on a novel polarization sensor for navigation. Pages 241–246 in *2007 International Conference on Information Acquisition*, held in Seogwipo-si, South Korea, 8–11 July 2007. Edited by J. Editor. City, St.: IEEE.

Chu, J., K. Zhao, Q. Zhang and T. Wang. 2008. Construction and performance test of a novel polarization sensor for navigation. *Sensors and Actuators A: Physical* 148 (1):75–82.

Cui, Y., J. K. Chu, N. N. Cao and K. C. Zhao. 2010. Study on measuring system for characteristics and distribution of skylight polarization. *Key Engineering Materials* 437:369–373.

Cui, Y., Q.-S. Gao, J.-K. Chu and C. Chen. 2013. Influence of sunlight and moonlight on polarization patterns during twilight. *Optics and Precision Engineering* 21 (1):34–39.

Fent, K. and R. Wehner. 1985. Oceili: a celestial compass in the desert ant Cataglyphis. *Science* 228 (4696):192–194.

Foster, G., A. Karastergiou, R. Paulin, T. D. Carozzi, S. Johnston and W. van Straten. 2015. Intrinsic instrumental polarization and high-precision pulsar timing. *Monthly Notices of the Royal Astronomical Society* 453 (2):1489–1502.

Hamaoui, M. 2017. Polarized skylight navigation. *Applied Optics* 56 (3):B37–B46.

Karman, S. B., S.Z.M. Diah and I. C. Gebeshuber. 2012. Bio-inspired polarized skylight-based navigation sensors: a review. *Sensors* 12 (11):14232–14261.

Lambrinos, D., R. Möller, T. Labhart, R. Pfeifer and R. Wehner. 2000. A mobile robot employing insect strategies for navigation. *Robotics and Autonomous Systems* 30 (1–2):39–64.

Liu, Z., R. Zhang, Z. Wang, L. Guan, B. Li and J. Chu. 2015. Integrated polarization-dependent sensor for autonomous navigation. *Journal of Micro/Nanolithography, MEMS, and MOEMS* 14 (1):015001.

Lu, H., K. Zhao, Z. You and K. Huang. 2015. Angle algorithm based on Hough transform for imaging polarization navigation sensor. *Optics Express* 23 (6):7248–7262.

Lu, H., K. Zhao, Z. You and K. Huang. 2017. Real-time polarization imaging algorithm for camera-based polarization navigation sensors. *Applied Optics* 56 (11):3199–3205.

Milione, G., H. I. Sztul, D. A. Nolan and R. R. Alfano. 2011. Higher- order Poincaré sphere, Stokes parameters, and the angular momentum of light. *Physical Review Letters* 107 (5):053601.

Pomozi, I., G. Horváth and R. Wehner. 2001. How the clear-sky angle of polarization pattern continues underneath clouds: full-sky measurements and implications for animal orientation. *Journal of Experimental Biology* 204 (17):2933–2942.

Pust, N. J., A. R. Dahlberg, M. J. Thomas and J. A. Shaw. 2011. Comparison of full-sky polarization and radiance observations to radiative transfer simulations which employ AERONET products. *Optics Express* 19 (19):18602–18613.

Tyo, J. S. 2002. Design of optimal polarimeters: maximization of signal-to-noise ratio and minimization of systematic error. *Applied Optics* 41 (4):619–630.

Vaughn, I. J. and B. G. Hoover. 2008. Noise reduction in a laser polarimeter based on discrete waveFigure rotations. *Optics Express* 16 (3):2091–2108.

Vedel, M., S. Breugnot and N. Lechocinski. 2011. Full Stokes polarization imaging camera. *Proceedings of SPIE* 8160:81600X.

Wang, Y., J. Chu, R. Zhang, L. Wang and Z. Wang. 2015. A novel autonomous real-time position method based on polarized light and geomagnetic field. *Scientific Reports* 5:9725.

Wu, T., Q. Tong, P. Pellikka, C. Zhang and L. Yan. 2018. Neutral point separation method for polarized effect between land objects and atmosphere in polarization remote sensing. *Journal of Remote Sensing* 22 (6):980–988.

Yan, L., X. Gu, J. Chu, Z. You, S. Liu, M. Hugh and V. Chandrasekar. 2018. Optical polarized effects for high-resolution quantitative remote sensing and new polarization remote sensing fields. *Journal of Remote Sensing* 22 (6):901–916.

Yan, L., G. X. Guan, J. B. Chen, T. X. Wu and X. Shao. 2009. The bionic orientation mechanism in the skylight polarization pattern. *Acta Scientiarum Naturalium Universitatis Pekinensis* 45 (4):616–620.

Zhang, W., Y. Cao, X. Zhang and Z. Liu. 2015. Sky light polarization detection with linear polarizer triplet in light field camera inspired by insect vision. *Applied Optics* 54 (30):8962–8970.

Zhang, Y., H. Zhao and N. Li. 2013. Polarization calibration with large apertures in full field of view for a full Stokes imaging polarimeter based on liquid-crystal variable retarders. *Applied Optics* 52 (6):1284–1292.

Zhang, Y., H. Zhao, P. Song, S. Shi, W. Xu and X. Liang. 2014. Ground-based full-sky imaging polarimeter based on liquid crystal variable retarders. *Optics Express* 22 (7):8749–8764.

Zhao, K., J. K. Chu, H. Y. Yao, Q. Zhang and T. S. Wang. 2007. Simulation and prediction for Rayleigh skylight polarization distribution. *Journal of Sichuan University: Engineering Science Edition* 39 (S1):287–291.